Article | Received 26 July 2025; Revised 4 October 2025; Accepted 5 October 2025; Published 8 December 2025
https://doi.org/10.55092/aimat20250015

Multi-scale modelling of mechanical responses of FeCrAl alloys with solid-solution and processing effects

Zhen Liu[1,2,†], Yaolin Guo[3,†], Jingyu Zhang[4,5,†], Yifan Li[2], Zheyu Hu[6], Muhammad Adnan[3,7], Nianxiang Qiu[8], Shurong Ding[5,*] and Shiyu Du[2,3,6,*]

[1] Ningbo Key Laboratory of High Performance Petroleum Resin Preparation Engineering and Technology, Ningbo Polytechnic University, Ningbo 315800, China
[2] College of Materials Science and Chemical Engineering, Harbin Engineering University, Harbin 150001, China
[3] Ningbo Institute of Materials Technology & Engineering, Chinese Academy of Sciences, Ningbo 315201, China
[4] State Key Laboratory for Turbulence and Complex Systems, Department of Mechanics and Engineering Science, BIC-ESAT, College of Engineering, Peking University, Beijing 100871, China
[5] Institute of Mechanics and Computational Engineering, Department of Aeronautics and Astronautics, Fudan University, Shanghai 200433, China
[6] School of Materials Science and Engineering, China University of Petroleum (East China), Qingdao 266580, China
[7] University of Chinese Academy of Sciences, Beijing 100049, China
[8] Yangtze Delta Region Institute (Huzhou), University of Electronic Science and Technology, Huzhou 313001, China

† These authors contributed equally to this work.

* Correspondence authors; E-mails: dingshurong@fudan.edu.cn (S.D.); 20220133@upc.edu.cn (S.D.).

Highlights:

- A multi-scale model for mechanical responses of Fe-Cr-Al alloys is proposed by coupling molecular dynamics, phase field and finite element method.
- The interaction between the solute atoms and screw or edge dislocations are considered in the MD-assisted solution strengthening models.
- The processing processes including rolling, recovery and recrystallization are simulated by the phase field models.
- The multiscale model supports the Materials Genome Initiative in alloy design through artificial neural network methods.

Abstract: A multi-scale computational model is proposed to calculate the mechanical responses of Fe-Cr-Al alloys with solid-solution and processing effects through a bidirectional coupling strategy. Based on crystal plasticity (CP) theory, a temperature-dependent critical resolved shear stress (CRSS) superposition model is constructed to couple with the molecular dynamics (MD), phase field model (PFM) and finite element method (FEM). By calibrating with few experimental data, we established an atom-informed solid solution strengthening model for multicomponent Fe-based alloys, thus successfully reproducing the polycrystalline features and stress-strain responses under different processing processes. Particularly, the multiscale model can provide high-precision yield strengths and reasonable tensile strength ranges for different grades of FeCrAl alloys. Finally, we present a case study employing an integration approach which starts from several experiment data, extends to hundreds of computational data and finally makes full-range prediction from artificial neural network methods. This study provides a viable and scalable scheme for the Materials Genome Initiative (MGI) design and optimization of nuclear-grade FeCrAl alloys.

Keywords: FeCrAl; mechanical responses; multi-scale calculation; Materials Genome Initiative; crystal plasticity; phase field; molecular dynamics; finite element method

1. Introduction

Owing to their excellent high-temperature corrosion resistance, FeCrAl alloys become one of the candidates for accident tolerant fuel (ATF) cladding materials [1,2]. With the gradual refinement of alloy grades, it is found that one of the bottlenecks restricting its application is the difficulty in precisely controlling the mechanical properties, including yield strength (YS) and ultimate tensile strength (UTS), which are of great significance for its resistance to swelling and burst in normal operation and accident scenarios [3,4]. However, it is difficult to establish a complete structure-property-process relationship by conventional experimental means. As the deformation mechanisms are revealed with more details at different scales in iron-based alloys, actually, it is now possible to establish a multi-scale model with a rational coupling strategy to directly calculate the properties under the framework of Material Genome Initiative (MGI) [5]. Therefore, it has become a hot topic to establish an easily calibrated and transferable multi-scale coupling algorithm for practical materials.

Crystal plasticity finite element model (CPFEM) [6,7] and visco-plastic self-consistent model (VPSC) [1] are two widely adopted homogenization models to predict the macroscopic mechanical properties by taking the microstructure and plastic deformation mechanism into account. Multiscale models with both CPFEM and VPSC have been adopted by researchers to study the plasticity of materials [8,9]. In order to better capture the physical mechanisms and make the parameters atomistically informed, CPFEM has been combined with molecular dynamics to investigate the plasticity of α-Fe [10] and high entropy alloys [11]. CPFEM and discrete dislocation dynamics (DDD) have been combined to investigate the hardening behaviors of materials [12]. Groh *et al.* [13] developed an MD-DDD-CPFEM multiscale model to capture the plasticity in aluminum. However, the microstructure evolution during processing such as rolling and annealing cannot be captured by these models.

The phase field method shows remarkable capabilities in the recrystallization organization evolution

and property prediction of alloys, providing a powerful tool for understanding and regulating the complex relationship between alloy microstructure and mechanical properties [14,15]. Therefore, this coupled model has a high potential to describe the microstructural evolution during the rolling and annealing of FeCrAl alloys. Recently, the Fast Fourier Transform (FFT) algorithm has been coupled with PFM for avoiding the mapping between finite element and finite difference grids, while preserving the high accuracy of CP results [16]. Zhao *et al.* [17] reported that the coupled FFT-CP and PFM can simultaneously describe the dynamic recrystallization in copper. Multiscale models combining PFM and CPFEM have also been proposed to capture the macroscale properties and the mesostructure evolution like twinning [18] and shear band [19]. An alternative approach is to couple kinetic Monte Carlo (kMC) with CPFEM [4]. However, new studies are also needed to combine atomic simulations with these multiscale models.

A multi-scale framework, covering the atomic scale to continuum level by first principles (FP), MD, PFM and FEM, has been proposed by Liu *et al*. [5] to calculate the thermo-mechanical properties of FeCrAl alloys. The framework provides a good idea on the multi-scale modeling by bottom-up method. However, due to the heavy computation in small length scale and parameter gap between models at different scales, no atomistic-based multi-scale model has successfully been adopted to capture the macroscale mechanical responses and microstructure evolution at the same time. A long-existing critical problem lies in how to bridge the models in different length and time scales. Moreover, models at intermediate scales often have many parameters that cannot be directly measured, making it difficult to be uniquely determined. Therefore, an effective multiscale model requires a robust coupling framework where all parameters can be determined using limited experimental data.

As a foundational theory with multi-scale capabilities, crystal plasticity is widely used to predict macroscopic stress-strain behavior by modeling the microscale mechanism of dislocation motion. Reflecting the microscopic mechanism of dislocation movements, in particular, the critical resolved shear stress is the key parameter related to specific materials and often decomposed into multiple contributions such as solid solution, grain boundary and work hardening [4,20]. Specifically, experimental test data of FeCrAl alloys show that their yield strength changes in three stages (I, II and III) with temperature [21], which is related to the changes in the dominant mechanisms of edge or screw dislocations at different temperatures and the evolution of the microstructure at high temperatures [22]. The solid solution contribution in alloys can often be obtained from the atomic scale, for instance, MD, by considering the interaction of dislocations with solid solution atoms [23,24]. Thus a composition-dependent computational model can be obtained [25,26]. The grain boundary and work-hardening contributions are very closely related to the mesoscopic structure and are expected to be obtained with the micro-structural evolution models, for instance, PFM [8]. Utilizing CRSS as a multi-scale bridge, it is possible to obtain the yield strength by CPFEM taking into account the polycrystalline structure and the heterogeneous mechanical field within the grains.

Consequently, we propose a practical multi-scale coupling model under the MD-PFM-FEM framework to predict the mechanical response of FeCrAl alloys. This model is calibrated with minimal experimental data and remains robust within a defined range, thereby providing reliable simulation data for the MGI design. A schematic of the multi-scale framework is presented in Figure 1, and its workflow is outlined below:

(1) Input Key MGI Factors: The model takes critical MGI parameters as inputs, including alloy

composition, test temperature and main parameters of processing conditions.

(2) Microscale Single-Crystal Plasticity: MD and solid solution models are employed to describe single-crystal plasticity at the atomic and defect scales.

(3) Mesoscale Microstructure Evolution: PFM and FFT-CP algorithm are used to simulate microstructure evolution and polycrystalline plasticity.

(4) Macroscale Mechanical Performance: CPFEM and homogenization techniques integrate the microstructural information to predict macroscopic mechanical behavior.

(5) Cross-Scale Consistency: CP theory serves as a unified foundation across all scales, ensuring self-consistency in modeling and parameter selection.

Furthermore, the UTS could be calculated by incorporating damage evolution models into the CPFEM based on the continuum damage mechanics [27,4]. MD has also been combined with FEM to investigate the fracture behavior of materials [28,29]. Following validation with experimental results from different compositions, the multiscale model will be applied to MGI design of FeCrAl alloys through a framework that integrates machine learning methods.

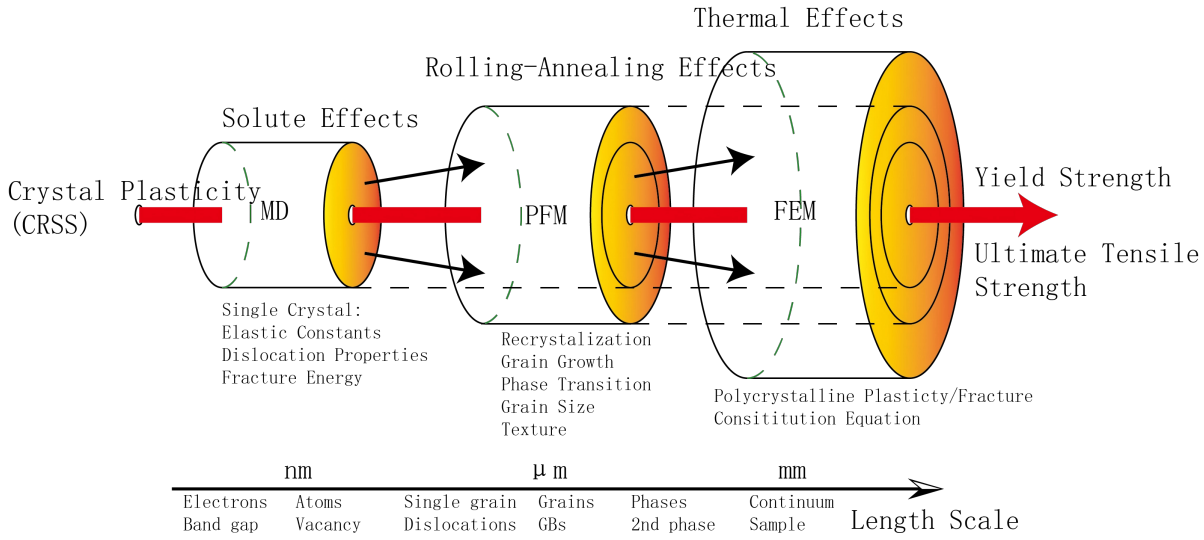

Figure 1. (Color online) Multi-scale coupling method for the calculation of yield strength and ultimate tensile strength.

2. Multi-scale coupling models

2.1. Damage-effect-involved CP coupling model

According to the classical crystal plasticity model, the velocity gradient $L(\mathbf{x})$ of the material point located at $\mathbf{x}$ in a deformed configuration is given as:

$$\mathbf{L}(\mathbf{x}) = \sum_{\alpha=1}^{N_\alpha} \dot{\gamma}^\alpha(\mathbf{x}) \left[\mathbf{n}^\alpha(\mathbf{x}) \otimes \mathbf{b}^\alpha(\mathbf{x})\right] \tag{1}$$

where α denotes a slip system and the sum runs over all N_α slip systems, $\mathbf{n}^\alpha$ is the normal vector of slip plane, $\mathbf{b}^\alpha$ is the Burgers vector, and $\dot{\gamma}^\alpha$ is the shear rate for the slip system α. Specifically, $\dot{\gamma}^\alpha$ is written as [4]:

$$\dot{\gamma}^\alpha = \dot{\gamma}_0 \left| \frac{\tau^\alpha}{(1-d)\tau_c^\alpha} \right|^{1/m} \mathrm{sgn}(\tau^\alpha) \tag{2}$$

where $\dot{\gamma}_0$ is a constant shear rate for referencing, τ^α is the resolved shear stress, and m is the strain rate sensitivity index. To obtain the ultimate tensile strength, in particular, a damping factor d is introduced to reflect the damage accumulation in stress-strain curves, obtained according to a damage evolution model and expressed as [4]:

$$d = \begin{cases} 0 & G \leq G_i \\ 1 - \exp(-\frac{G-G_i}{G_c-G_i}) & G > G_i \end{cases} \tag{3}$$

where $G = \sum_{\alpha=1}^{N} \int_0^t \frac{\tau^\alpha \dot{\gamma}^\alpha}{1-d} \mathrm{d}t$ is the effective plastic work, G_i is the initial plastic work, G_c is the plastic work at fracture when d is approaching unity [4]. τ_c^α is the critical resolved shear stress, expressed as:

$$\tau_c^\alpha = \tau_0^\alpha + \int \sum_{\beta=1}^{N_\beta} h_{\alpha\beta} |\dot{\gamma}^\beta| \mathrm{d}t \tag{4}$$

where τ_0^α is the initial CRSS, the time-integral term is the cumulative work hardening stress, and $h_{\alpha\beta}$ is the interaction strength between α and β slip systems, written as:

$$h_{\alpha\beta} = q_{\alpha\beta} h_0 \left| 1 - \frac{\tau^\beta}{\tau_s} \right|^a \mathrm{sgn}\left(1 - \frac{\tau^\beta}{\tau_s} \right), (\text{no sum on } \beta) \tag{5}$$

where $q_{\alpha\beta}$ represents an interaction coefficient between different slip systems, h_0 is the initial hardening rate, a is the softening exponent, and τ_0^α is the saturation stress.

Particularly, a multi-factor superposition model for τ_0^α is established by considering the contribution from solid solution, grain boundary and work hardening effects for the FeCrAl alloys, so the expression of τ_0^α is proposed to be:

$$\tau_0^\alpha(T, c, \tilde{A}, d_g) = \tau_{sol}^\alpha(T, c) + \tau_{HP}^\alpha(T, d_g) + \tau_{Ha}^\alpha(T, \tilde{A}) \tag{6}$$

where $T, c, \tilde{A}, d_g$ refer to the temperature, atomic component, characterized work hardening coefficient and average grain diameter, and $\tau_{sol}^\alpha(T, c)$, $\tau_{HP}^\alpha(T, c)$ and $\tau_{Ha}^\alpha(T, c)$ denote the solute hardening, grain boundary and work hardening contribution, respectively.

2.1.1. Solute solution hardening

It is assumed that three-stage expression of the CRSS solid solution term is controlled by thermally activated screw dislocations in the low temperature stage, edge dislocations in the mid-temperature stage, and the failure of the dislocation mechanism decreases rapidly at high temperatures due to dislocation climbing and other reasons. The solute hardening term τ_{sol}^α is considered as the competition of screw/edge migration mechanisms varying with temperature, expressed as:

$$\tau_{sol}^\alpha(T, c) = \frac{\mu(T)}{\mu(0)} \max\{\tau_{screw}^\alpha(T, c), \tau_{edge}^\alpha(T, c)\} f(T) \tag{7}$$

where μ is the shear modulus and $\tau_{screw}^\alpha(T, c)$ (or $\tau_{edge}^\alpha(T, c)$) denotes the solute strengthening strength dominated by screw (or edge) dislocations. In this study, Argon's model [25] and Maresca's model [30] are adopted to estimate $\tau_{screw}^\alpha(T, c)$ and $\tau_{edge}^\alpha(T, c)$, respectively. The detailed formula for these solute hardening models are listed in Appendix A. $f(T)$ is a phenomenological attenuation function to describe

the fast decay of τ_0^α at high temperatures (Stage III), expressed as:

$$f(T) = \frac{1}{2}\left(1 + \tanh\left(-\frac{T - T_h}{S_0}\right)\right) \tag{8}$$

where T_h is the transition temperature and S_0 is a characterized decaying range. The truncation function of $f(T)$ has little effect on Stage I and II.

2.1.2. Grain boundary hardening and other hardening effects

The grain boundary hardening τ_{HP}^α is described by the Hall-Petch relation as:

$$\tau_{HP}^\alpha(T, d_g) = \frac{\mu(T)}{\mu(0)} \tilde{k}_{GB} \cdot {d_g}^{-0.5} f(T) \tag{9}$$

where $\tilde{k}_{GB}$ is the Hall-Petch coefficient, and should be obtained by experiment. The temperature dependency of τ_{HP}^α is the same as those of the shear modulus [4]. $f(T)$ is also included in the model to consider the break-down of Hall-Petch effect at high temperature. d_g is average grain diameter, which depends on the processing conditions and can be obtained by PFM.

The work hardening term $\tau_{Ha}^\alpha(T, \tilde{A})$ is generally considered to be of long-range and represented as:

$$\tau_{Ha}^\alpha(T, \tilde{A}) = \tilde{A}\mu(T) \tag{10}$$

where $\tilde{A}$ denotes a work hardening coefficient and is closely related to heat treatment conditions with different mechanisms of microstructural evolution. For instance, $\tilde{A}$ can be very high during the rolling process and become zero when the complete recrystallization is achieved. Note that $\tilde{A}$ does not change with temperature, which plays as a key factor for the hardening term to convert between different temperatures. For this term, PFM should be combined with CP and recovery models to reproduce the changes in $\tilde{A}$ with various thermo-mechanical processing, which is detailed in Appendix B.

2.1.3. Other parameters

Also, the temperature dependency of h_0 and τ_s^α in Equation (5) are taken into account in our model. h_0 is regarded to vary with temperature as shear modulus does, namely:

$$h_0(T) = \lambda\mu(T) \tag{11}$$

where λ is a constant coefficient. Taking τ_0^α as a reference, the expression of saturation CRSS τ_s^α is written as:

$$\tau_s^\alpha(T, c, d_g) = \tau_{sol}^\alpha(T, c) + \tau_{HP}^\alpha(T, d_g) + \tau_{sh}^\alpha(T) \tag{12}$$

where τ_{sh}^α represents the saturation CRSS induced by the dislocation interactions, assumed to be proportional to shear modulus at low temperatures ($T \leq 0.3T_m$, T_m represents the melting temperature in K) and decrease quickly at high temperatures [31], expressed as:

$$\tau_{sh}^\alpha = \begin{cases} \chi\mu(c, T) & T \leq 0.3T_m \\ \tau_{s0}\left[\frac{\dot{\varepsilon}_0}{A}\exp\left(\frac{Q}{RT}\right)\right]^{n_s} & T > 0.3T_m \end{cases} \tag{13}$$

where A is a pre-exponential factor, Q is the activation energy, n_s is the strain rate sensitivity parameter, τ_{s0} is the reference saturation CRSS, χ is a correction constant, and R is the gas constant and $\dot{\varepsilon}$ is the loading rate.

In addition, a complete expression for G_i and G_c in the damage evolution model needs to consider the function of the plastic work within each grain as a function of factors such as composition, temperature, and processing. In this study, their relationships with composition-dependent plastic work $G_{i0}(c)$ in single crystals are expressed as:

$$\begin{aligned} G_i &= f_i(\tilde{A}_{harden}, T) \cdot G_{i0}(c) \\ G_c &= f_c(\tilde{A}_{harden}, T) \cdot G_{i0}(c) \end{aligned} \tag{14}$$

where $G_{i0}(c)$ can be obtained from MD simulation, $f_i(\tilde{A}_{harden}, T)$ and $f_c(\tilde{A}_{harden}, T)$ represent the correction factors depending on the test temperature and work hardening coefficient determined by processing conditions. The damage model is also adopted in CPFEM to obtain the stress-strain curves, as detailed in Appendix C.

2.2. *Coupling strategy for the multi-scale simulations*

In order to achieve as seamless connection of cross-scale parameters as possible, we divided the coupling parameters into three types. The first is the directly transferred parameters that consider simple mechanisms such as elastic constants, grain boundary energy, and poly-crystalline structure, the second is the CRSS parameters involving multiple physical mechanisms, and the third is the phenomenological coupling parameters of ambiguous mechanisms, such as fracture energy G_c and G_i. Figure 2 shows the relationship of the three types of coupling models and the transport paths of coupling parameters.

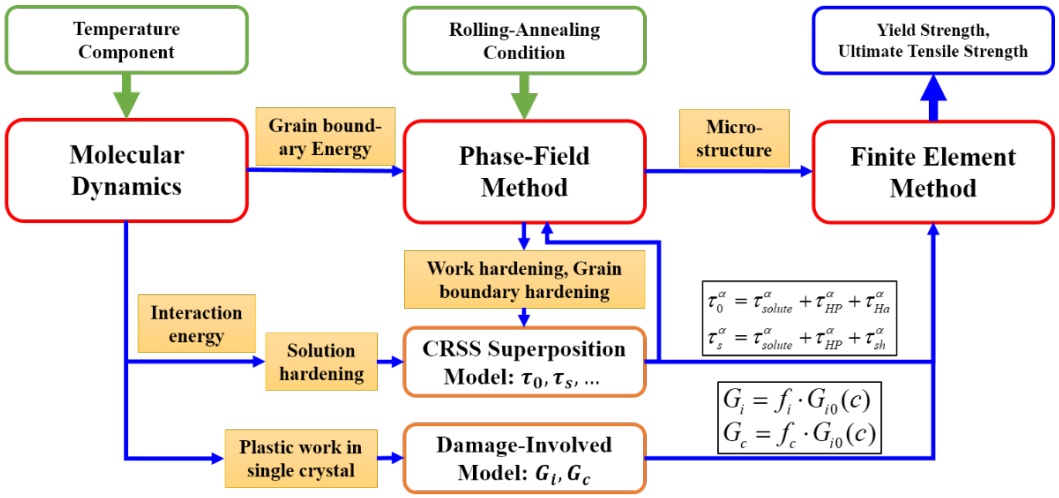

Figure 2. Multi-scale coupling strategy for multiscale simulations by MD-PF-FEM considering the temperature, component and rolling-annealing effects.

First, MD is used to construct the atomic structures of various defects, such as single crystal, solutes, screw/edge dislocations[32,33] and symmetric tilt grain boundaries[34], to estimate their properties as a function of components and temperature via the open-source software LAMMPS. The most challenge work of MD is to calculate the solute-dislocation interaction energies, which determine the solute strengthening ability of various elements. The energy calculations are organized at 0K with molecular statics method

and the conjugate gradient (CG) algorithm are used for energy minimization. The temperature dependent parameters, such as the grain boundary energy $\gamma_{GB}(T)$ and G_{i0}, are measured with the NPT ensemble for sufficient relaxation. Considering the effects of solute randomness, the MD simulations are repeated at least 10 times to obtain the average value and error limit. The MD results will be used to construct solid solution strengthening models and partly parameterize the phase field and finite element methods, *etc*.

Second, the solution of the phase field method coupled with crystal plasticity is conducted by the home-made program PHAFIS [35]. For the rolling process, FFT-CP algorithm is applied to numerically simulate the accumulation of plastic strain and increments of τ_0^α, consistent with the reference [36]. The recovery and phase-field equations are solved by Euler forward integration methods. Additionally, the efficient algorithm proposed by Kim *et al*. [37] is employed to accelerate the numerical PFM simulations. The initial 3D polycrystalline structure is constructed by the Voronoi algorithm with periodic boundary conditions in all three dimensions. In terms of parameter determination, the interface energy, Debye frequency, and elastic constants are obtained directly from MD simulations. A few parameters left that are difficult to calculate, such as high temperature saturation stress and recovery activation volume, *etc*., which are determined by parameter identification according to some specific experiments. The phase field output results include 3D polycrystalline structure data (orientation, centroid, grain size of each grain), work hardening coefficient, etc., which are transmitted to FEM in the form of files.

In CPFEM, third, the models are implemented in the finite element software Abaqus/Explicit. Based on the numerical implementation algorithm detailed in our previous research [4], a user-defined VUMAT subroutine in Fortran is written to describe the constitutive model in each integration point using the CRSS model and damage model. Periodic boundary conditions and velocity boundary conditions are applied on the representative volume element (RVE). In the transfer of microstructure, as the mesh number in FEM may be different from that in PFM, the grain morphology and orientations in PFM could not be directly transferred to FEM. According to the coordinates of each integration point in FEM, the corresponding grid element in PFM can be obtained and they have the same grain orientation. After the calculation of Abaqus, a python script is programmed to obtain the homogenized stress-strain curve automatically together with the yield strength and ultimate tensile strength.

3. Results

In order to obtain the mechanical properties consistent with the experimental results, the model and transfer parameters of each method need to be determined comprehensively. Firstly, with the available related data for similar iron base alloy from literature, it is necessary to determine the sensitivity of parameters to components, temperature and processing conditions, then obtain the reasonable value range. Secondly, the atomic scale simulations are applied to obtain the physical properties of microscale defects (solute substitution defects, dislocations, grain boundaries), which are helpful to understand the microscale mechanisms and their relationship with macroscale properties, providing bottom-up information for model verification. Furthermore, a few customized experiments are organized to provide necessary top-down reference for determining the phenomenological parameters for the intermediate scale models. Finally, with the input alloy composition, processing and testing conditions, multi-scale coupling calculation is automatically realized by programming and outputting the stress-strain curve, yield strength and UTS for the poly-crystalline alloys.

3.1. Parameters calibration with experimental data (CPFEM top down)

In order to verify the multi-scale coupling model, experimental data for Fe-13Cr-5Al-2Mo-0.2Si-0.05Y (in nominally component of wt.%) alloys with the same preprocessing of melting and rolling but different annealing treatments are adopted [4], denoted as Sample I, II, and III. Sample I was directly cooled to room temperature without annealing, and Sample II and Sample III were annealed at 600 °C and 800 °C for 1 hour, respectively. The three samples all shows BCC crystal structure according to the X-ray diffraction (XRD) results, and their average grain diameters are 43.7 ± 10.9 μm (Sample I), 45.2 ± 11.4 μm (Sample II) and 32.0 ± 14 μm (Sample III), respectively. Considering the grains in Sample III are obviously refined and equiaxed, it is assumed that complete recrystallization occurs. Compared to Sample I, the grain size of Sample II is slightly larger, but the grain morphology is more irregular, indicating recovery mechanism might be dominant at this time [4].

Figure 3 shows the schematic evolution of τ_0^α with processing conditions. During the rolling at 800 °C, τ_0^α gradually increases and eventually approaches a saturation value, as shown by the AB segment in the figure. After cooling to room temperature, τ_0^α is expected to increase rapidly, as shown by the BC segment. For 800 °C annealing, the recrystallization process causes τ_0^α to reach a lower value at room temperature, as shown by the BE segment. For the 600 °C annealing process, τ_0^α is between the other two CRSS at room temperature. Ideally, the three samples contain exactly the same solid solution strengthening fraction (component controlled), with the main difference being that Sample III has a zero work-hardening fraction and Sample II has a smaller work-hardening contribution than Sample I.

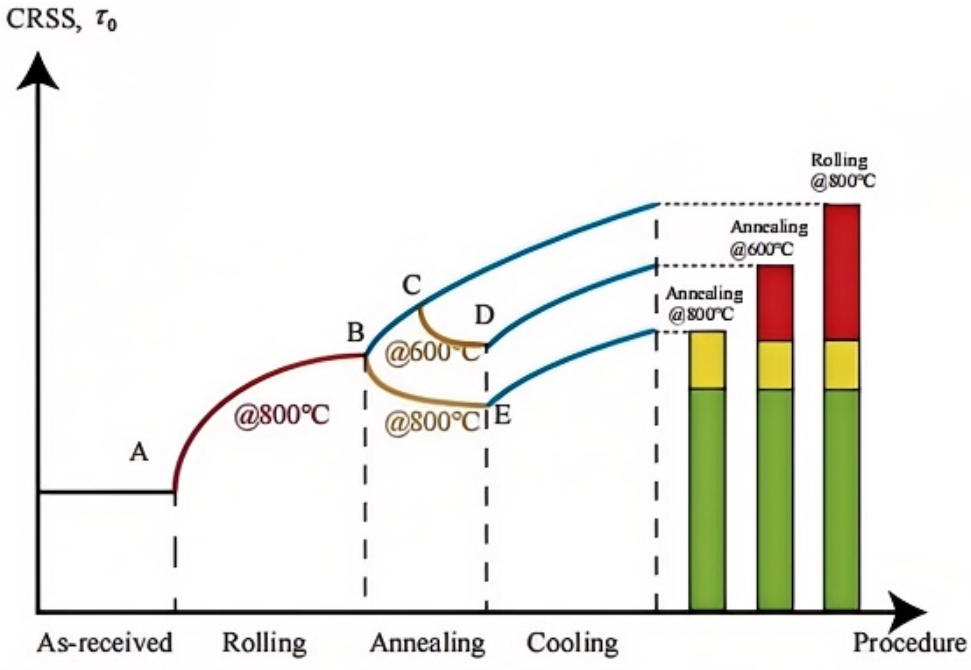

Figure 3. Effects of processing conditions on the evolution of initial CRSS.

CPFEM alone is firstly performed to fit the three stress-strain curves of the above mentioned FeCrAl samples to provide a reference for the parameters in the models at the lower scale, and the details can be found in our previous work [4]. The calibrated parameters are shown in Table 1. 48 slip systems belonging to $\{110\}\langle111\rangle$, $\{112\}\langle111\rangle$ and $\{123\}\langle111\rangle$ are considered. The elastic constants as a function

of temperature are fitted based on the experimental data of the elastic modulus of FeCrAl alloys, as shown in Supplementary Material S1. The initial CRSS τ_0^α, and parameters for plastic work (G_i and G_c) vary with processing conditions. Based on the CPFEM results of Sample III, the relation between yield strength σ_{YS}(MPa) and τ_0^α(MPa) is fitted as $\sigma_{YS} = 2.4\tau_0^\alpha + 19.5$, where 2.4 is the Taylor factor. According to the CRSS model and Hall-Petch coefficient $\tilde{k}_{GB}$ (*i.e.*, $\tilde{k}_{GB} \cdot \mu(300\ \mathrm{K}) = 215.52\ \mathrm{MPa} \cdot \mu\mathrm{m}^{0.5}$), τ_{sol}^α of the three samples is calculated as 147 MPa, acting as a reference for the parameter identification in the following solution strengthening models.

Table 1. Model parameter calibrated by CPFEM at room temperature.

Symbol	Definition	Value	Source
$\dot{\gamma}_0$ (s^{-1})	Reference shear strain rates	0.001	[4]
m	Strain rate sensitivity coefficient	0.012	[4]
$q^{\alpha\beta}$	interaction parameter between slip system α and β	1.0 if $\alpha = \beta$; 1.4 for other cases	[4]
a	Softening coefficient	2.25	[4]
τ_s (MPa)	Saturation CRSS	900	Fit to Experiment
h_0 (MPa)	Initial hardening rate	300	Fit to Experiment
k_{HP} (MPa·$\mu m^{1/2}$)	Hall-Petch coefficient for CRSS	215.2	Fit to Experiment
τ_0 (MPa)	Initial CRSS for FEM	S_I: 282 S_{II}: 240 S_{III}: 185	Fit to Experiment
G_i (10^6 J/m^3)	Plastic work initiating damage	S_I: 40 S_{II}: 55 S_{III}: 60	Fit to Experiment
G_c (10^6 J/m^3)	Plastic work at fracture	S_I: 230 S_{II}: 230 S_{III}: 680	Fit to Experiment

Note: S_I: Sample I; S_{II}: Sample II; S_{III}: Sample III.

3.2. Solute effects on plasticity and fracture in single crystals (MD bottom-up)

The MD method studies the impact of defects such as solute atoms on micro-mechanical properties through atomic-level simulations, thereby providing component correlation parameters from a bottom-up perspective. In the Argon's screw dislocation hardening model, the characteristic energy is the solute-kink interaction energy ΔU_{screw}^X. Figure 4a shows the double-kink structure optimized by MD and energy barriers for Cr, Al in left or right kinks are shown in Figure 4b. As a result, MD calculated ΔU_{screw}^X for Cr and Al are 0.050 and 0.049 eV, respectively. On the other hand, the corresponding ΔU_{screw}^X deduced from experimental data [3] are 0.038 and 0.055 eV. These results show that the ΔU_{screw}^X from MD double-kink structures are in the same magnitude with the experiment deduced value for Argon's model. However, it is still difficult to quantitatively calculate ΔU_{screw}^X by MD or DFT directly [38] and misfit coefficient models may be a potential solution [39]. According to the slope of yield strength or CRSS from experiment [3,40,41], ΔU_{screw}^X for Cr, Al, Mo, Si are taken as 0.038, 0.055, 0.075 and 0.075 eV, respectively. However, with the current component Fe-13Cr-5Al-2Mo-0.2Si wt%, the CRSS at 300 K is higher than the top-down value 147 MPa. Therefore, the alloy component is artificially adjusted to be Fe-12.68Cr-4.7Al-1.92Mo-0.2Si wt%, which enables a higher degree of integration between the theoretical model and experimental results and continues to be used in subsequent analyses.

In the Maresca's edge dislocation hardening model, the characteristic energies $\Delta\tilde{E}_p^X$ are estimated based on the solute-dislocation binding energy $U_{dis}^X(\mathbf{r})$ near the edge dislocation core. Since for edge dislocations the volumetric term makes the main contribution to $U_{dis}^X(\mathbf{r})$ and the chemical term is

neglectable [30], alternatively, the volumetric misfit approximation (VMA) model [42] is proposed to reduce the dependency on interatomic potentials. Figure 4c shows the edge core structure constructed by MD and the comparison of MD and VMA model calculated $\Delta\tilde{E}_p^X(w_e^{crit})$ is shown in Figure 4d. The VMA estimated $\Delta\tilde{E}_p^X(w_e^{crit})$ is a little lower than the MD results, which indicates VMA model is a feasible model instead of MD simulations. Most importantly, the VMA model can combine the size misfit parameter ε_a^X from other reliable sources, despite the drawbacks of Fe-X binary potentials such as inaccuracy and absence. Utilizing the experiment measured ε_a^X for Cr, Al, Mo and Si [43], the corresponding $\Delta\tilde{E}_p^X(w_e^{crit})$ from the VMA model are 0.283, 0.856, 1.777 and 0.332 eV, respectively. The fitted parameters in the solute hardening models are listed in Table 2 and the CRSS curve considering the solute hardening and grain-boundary hardening effects is shown in Figure 4e. The predicted CRSS curve is closely fitted to the experimental measured results, which provides the basic input for simulations at the higher scale, and also provides the expansion possibility for temperature and composition in the multi-scale model.

In addition, the MD calculated microscale fracture energies and grain boundary energies are in the same magnitude with macroscale values. The details of MD simulations are listed in Supplementary Material S2.

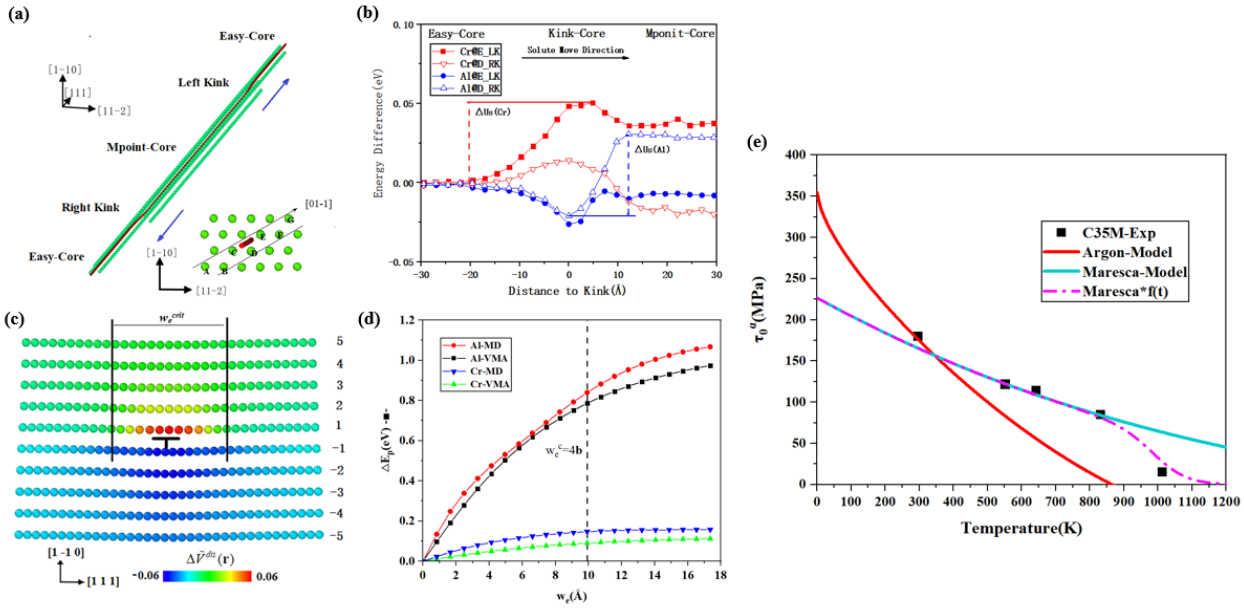

Figure 4. Determination of parameters in solute hardening models by MD simulations. **(a)** Atomic structure of 1/2<111> screw kink-pair; **(b)** Energy barrier for kink migration over single substitutional defects; **(c)** 1/2<111>{110} edge dislocation core structure and the volumetric strain distributions; **(d)** $\Delta\tilde{E}_p^X(w_e^{crit})$ curves calculated by MD and VMA models; **(e)** Three-stage CRSS curves compared with the experiment data for C35M alloy [44].

Table 2. The determined parameters for CRSS solution hardening models. The experimental results are from [44].

Symbol	Definition	Value	Source
b	Burgers vector length	2.46 Å	[25]
w_s	Substitution-screw dislocation interaction range	2.31 Å	[25]
$\tau^{ath}_{screw,Fe}$	Athermal lattice resistance stress for pure iron	21 MPa	[25]
$\ln(\dot{\varepsilon}_0/\dot{\varepsilon})$	Strain rate coefficient	20	[26]
λ_s	Peierls valley distance	2.31 Å	[38]
w_k	kink-pair twist width	20 b	[38]
Γ_e	Edge dislocation Line Tension	1.6 eV/Å	Fit to Experiment
$\hat{\tau}_e(0)$	Edge dislocation Peierls stress	40 MPa	Fit to Experiment
T_h	Transition temperature	1000 K	Fit to Experiment
S_0	Characterized decaying range	100 K	Fit to Experiment
ΔU^{Cr}_{screw}	Screw migration energy barrier with single Cr substitution	0.038 eV	Fit to Experiment
ΔU^{Al}_{screw}	Screw migration energy barrier with single Al substitution	0.055 eV	Fit to Experiment
ΔU^{Mo}_{screw}, ΔU^{Si}_{screw}	Screw migration energy barrier with single Mo or Si substitution	0.075 eV	Fit to Experiment
$\Delta\tilde{E}^{Cr}_p(w^{crit}_e)$	Characteristic energy for Cr pinning effect on edge	0.283 eV	VMA evaluated
$\Delta\tilde{E}^{Al}_p(w^{crit}_e)$	Characteristic energy for Al pinning effect on edge	0.856 eV	VMA evaluated
$\Delta\tilde{E}^{Mo}_p(w^{crit}_e)$	Characteristic energy for Mo pinning effect on edge	1.777 eV	VMA evaluated
$\Delta\tilde{E}^{Si}_p(w^{crit}_e)$	Characteristic energy for Si pinning effect on edge	0.332 eV	VMA evaluated
w^{crit}_e	Substitution-edge dislocation interaction range	9.9 Å	MD calculated
G_{i0}	Microscale plastic work	1.65×10^8 J/m^3	MD calculated
$\gamma_{GB}(T)$	Grain boundary energy	See Supplementary Material S2.1	MD calculated

3.3. Polycrystalline structure after rolling-annealing processes (PFM connect)

In order to obtain the polycrystalline structure after different processing techniques, some assumptions are necessary to be made as follows. The rolling process modeled by the FFT-CP model for the three samples is exactly the same, and the difference between them comes from the subsequent annealing process. During the rolling modelling, only the accumulation of the stress-strain field is considered, ignoring the microstructure changes such as grain boundary migration. Directly cooled to room temperature without annealing, the CRSS of Sample I increases with the decrease of temperature according to Equation (7), while the structure remains unchanged (the average grain size is always 43.7 μm). Based on the polycrystalline structure after rolling, the recovery simulation is carried out to describe the evolution of CRSS in Sample II by Equation (B.2) in Appendix B. On the other hand, Sample III requires PFM to simulate static recrystallization with the plastic strain field from FFT-CP as the driving force.

The model parameters of room temperature CPFEM are inherited as much as possible into the simulation of high temperature rolling at 800 °C. The initial polycrystalline structure is shown in Figure 5a. The only unknown parameter is the saturation CRSS τ_s, which can be constrained by $\tilde{A}^{rolling}_{harden}$ given by the CRSS superposition model and the expected $\tilde{A}^{rolling}_{harden}$ is approximately 80 MPa at 800 °C. First, the total CRSS and solid solution strengthening at room temperature give $h = 1.3 \times 10^{-3}$, leading to $\chi = 0.009043$ in Equation (13). Next, Equation (6) yielded the target CRSS for rolling, $\bar{\tau}^{roll}_{\alpha} = 80$ MPa. Finally, we

iteratively adjusted τ_s in FFT-CP simulations until achieving this target. Figure 5b displays the strain distribution at 60% deformation, which corresponds to the identified saturation stress of $\tau_s = 88.7$ MPa.

For Sample II after annealing at 600 °C, it mainly involves the identification of recovery activation parameters. Generally, iron-based alloys play a dominant role in vacancy diffusion during recovery, and the recovery activation energy is about 2.9 eV, so the recovery activation volume is the only undetermined parameter. Similar with the above case, after some attempts, we got the result that when $v = 26.2b^3$ (denoted as v_0) the average CRSS after one hour is exactly 112 MPa. Figure 5c shows that average CRSS is dependent on the activation volume parameters. Martinez *et al.* [45] pointed out that the activation volume of Fe-3% is 30–36b^3 based on the self-diffusion mechanism. More recently, avrikakis *et al.* [46] fixed the activation volume as $12b^3$ to fit the activation energy, which is found to be between 2.5–3.0 eV for Fe-3% doped with Sn. Considering that Fe-Cr-Al and Fe-Si share the same BCC structure and the similarity of the vacancy diffusion mechanism at high temperatures, the activation parameters obtained are within a reasonable parameter range.

For the recrystallization simulation, the microstructure after recrystallization nucleation is shown in the Figure 5d. The grain boundary energy can be obtained directly from the results of the MD fitting, and the width is set to $5\Delta x$. Figure 5e,f show the polycrystalline morphology just after recrystallization and with 1 hour's grain growth. Specifically, 5% of stored energy is adopted to drive the annealing process in the following simulations, resulting in the average stored energy being on the scale of 1 MPa, which is reasonable for iron-based alloys [47]. By identifying the grain boundary mobility to be 1.34×10^{-13} m^4/Js, an average grain size of 32 ± 13 μm is obtained after 1 hour's annealing. Based on the limited experimental data, CPFEM fitting results, and solid solution effect parameters, all the parameters related to the phase field-crystal plasticity model are calibrated, are shown in Table 3.

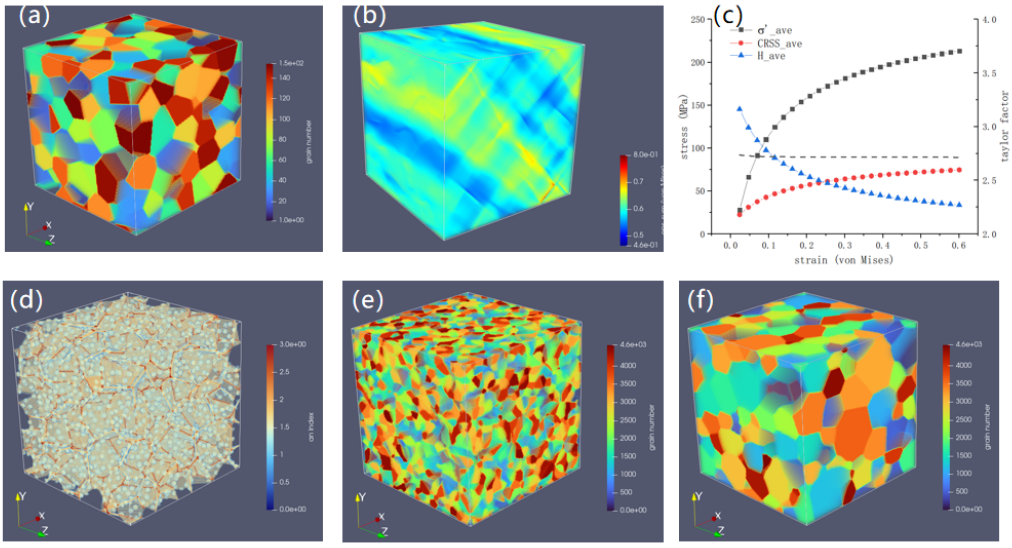

Figure 5. Polycrystalline morphology and plastic responses at the mesoscopic scale. **(a)** Initial polycrystalline structure, **(b)** average deviatoric stress, average CRSS and equivalent hardening factor as well as Taylor factor varying with von Mises strain; **(c)** Variation of average CRSS with time with different activation volume parameters; Snapshots of **(d)** recrystallization nucleation, **(e)** polycrystalline morphology just after recrystallization is completed; **(f)** Polycrystalline morphology with 1 hour's grain growth.

Table 3. Parameters determination for PFM.

Symbol	Definition	Value	Source
h_0	Initial hardening coefficient	199 MPa	CPFEM Top down
a	Softening coefficient	2.25	CPFEM Top down
n	Strain sensitivity index	83	CPFEM Top down
γ	Grain boundary energy	0.90 J/m^2(1073 K)	MD Bottom up
b	Magnitude of Burgers vector in FeCrAl	0.245 nm	MD Bottom up
ω	Debye frequency	8.57e12 s^{-1}	MD Bottom up
U_0	Activation energy for recovery	2.9 eV	MD Bottom up
τ_s	Saturation stress	88.7 MPa	Fit to Experiment
v	Activation volume for recovery	$26.2b^3$	Fit to Experiment
M	Grain boundary mobility	1.34e-13 m^4/Js	Fit to Experiment
λ	Excess free energy scaling factor	5%	Fit to Experiment

3.4. MD-PFM-FEM coupled calculation

A set of multi-scale model parameters for FeCrAl alloys have already been obtained, and each of them has been validated to some extent or at least within reasonable ranges. Using the complete coupling strategy in Figure 2, the mechanical responses of three FeCrAl samples are obtained in a hierarchical way by MD-PFM-FEM coupled calculation. Table 4 shows the input parameters of the multiscale calculation, and the parameters are passed into MD, PFM or FEM. As FEM relates the properties of single crystal and mesostructure to macroscale properties, we further display its input and outputs, as shown in Figure 6. The polycrystalline morphology is simulated by PFM and passed into FEM, as displayed in Figure 6a,b. Although the mesh number in FEM is less than that in PFM, the macroscale mechanical responses including convergent stress-strain curves can be well captured. It is noted that the grain morphology of Sample II is duplicated from that of Sample I, but the average grain size is uniformly enlarged to 45.2 μm. There are no significant textures and the associated texture strengthening, from the pole figures shown in Figure 6c,d. More importantly, the two samples show clear discrepancies with respect to the initial CRSS (τ_0^α), indicated by the distribution of work hardening coefficient ($\tilde{A}_{harden}$), as shown in Figure 6e. As expected, the values of $\tilde{A}_{harden}$ in Sample II are lowered due to the recovery process, than that of Sample I. Compared with the results of Samples I and II, there is stronger grain boundary hardening with smaller grain diameter in Sample III, but no work hardening effects are involved because of the occurrence of full recrystallization therein.

Table 4. Input parameters for the multiscale coupling model.

Parameter	Value	Model
Alloy component	Fe-12.68Cr-4.7Al-1.92Mo-0.2Si (wt%)	MD
Initial microstructure	Grain size 43.7 ± 10.9 μm and random orientation	PFM
Thermal treatment	Sample I: warm-rolling at 1073 K with 60% thickness reduction	PFM
	Sample II: warm-rolling at 1073 K with 60% thickness reduction, annealing at 873 K for 1 h	
	Sample III: warm-rolling at 1073 K with 60% thickness reduction, annealing at 1073 K for 1 h	
Test condition	Tensile rate 0.001 s^{-1} at 300 K	FEM

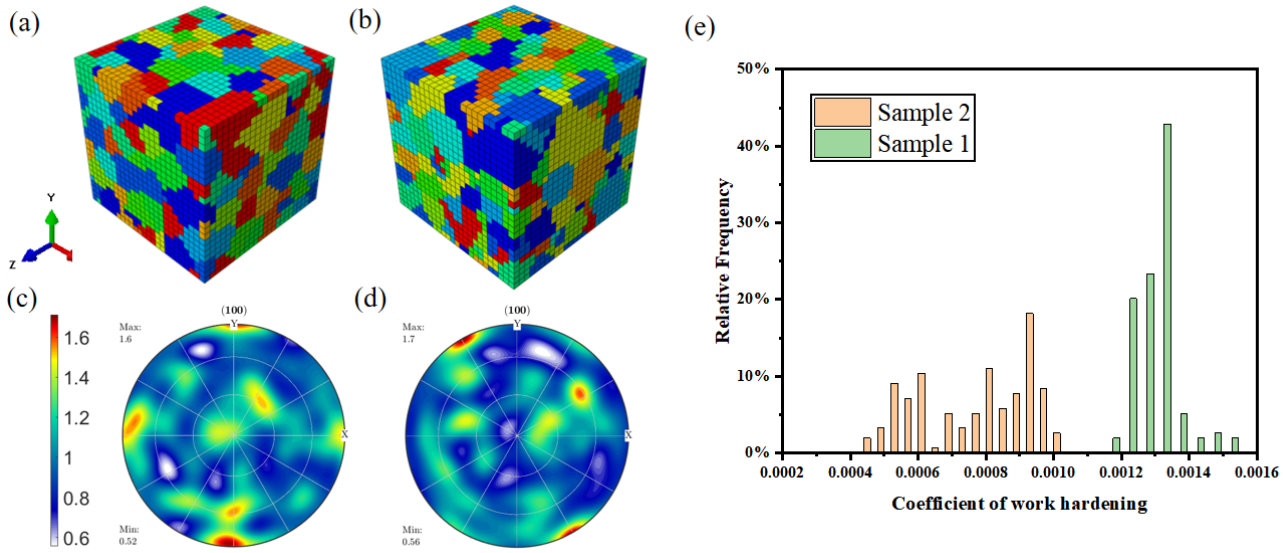

Figure 6. The input structures for FEM model. **(a,b)** Polycrystalline morphology constructed by FEM for Sample I and Sample III; **(c,d)** Pole figure of the initial orientations of Sample I and Sample III; **(e)** Distributions of the work hardening coefficient ($\tilde{A}_{harden}$) passed from PFM to the coupled transfer model.

The results of multiscale simulations are compared with experimental data, as displayed in Figure 7. The homogenized stress-strain curves for the three samples agree very well with the experimental data. By comprehensively considering the effects of solid solution hardening, grain boundary hardening, working hardening, strain hardening, and strain softening, therefore, our multiscale framework shows its capability to model the mechanical response of FeCrAl alloys with different processing conditions. The multiscale model is further validated by comparing the predicted yield strength with experimental data of similar Fe-13Cr-5Al alloys at different temperatures, as shown in Figure 7b. The C35M alloys by [1] have the same alloy compositions and mesostructure as those of Sample III. The parameters for the C35M-2 alloy by [44] are the same as those of Sample III except the alloy compositions and grain size. For the T35Y2 (Fe-13.15Cr-4.44Al-0.12Y wt.%) alloy by [44], it is assumed that complete recrystallization occurs according to the fact that the alloy was hot-extruded at 1050 °C and annealed at 700 °C for 1 h. An average grain diameter of 65 μm is adopted. It is found that the yield strength predicted by multi-scale simulations agrees well with the experimental data at different temperatures in Stage I, II and III, which proves the effectiveness of the temperature-dependent CRSS model and current multi-scale model. The simulation results also show that the Taylor factor is about 2.4 at all the considered temperatures, which agrees with the value obtained by FEM in Section 3.1. Therefore, it is reasonable to use this value to estimate the yield strength when determining the parameters of solid solution hardening.

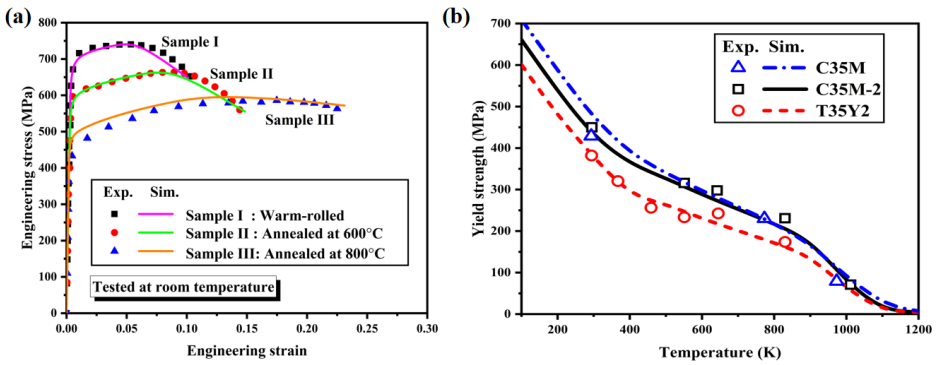

Figure 7. Comparisons of multiscale simulation results with experimental data: **(a)** stress-strain curves at room temperature of the samples after different processing conditions; **(b)** Yield strength of C35M [1], C35M-2 [44] and T35Y2 [44] alloys at different temperatures.

4. Applications

4.1. Validation with other experiments

In order to test the scalability of this model, the experimental data of FeCrAl alloys from [44,48] are adopted to validate the model. Since all the samples have undergone rolling and annealing above 700 °C, which can be considered to be in a fully recrystallized state with different grain sizes, the parameters for Sample III are adopted for these samples while the components and grain size are varied according to the experiments. The comparisons of the predicted YS and UTS with the experimental data are shown in Figure 8. It can be seen that the YS and UTS of the smaller grain samples are greater than those of the larger grain specimens, correctly reflecting the phenomenon of fine grain strengthening. One of the most striking results is that the difference between the predicted and experimental values of YS at room temperature is only 13.1%, regardless of grain size or component variation (11-15Cr, 2-6Al), indicating that our model correctly reflects the pattern of component and grain size effects on YS at room temperature. At 550 K, the limited data indicate that the yield strength is underpredicted by up to 27.8% for the large-grain samples from [44], whereas the underprediction is up to 11.1% for the small-grain Alkrothal-14 alloy.

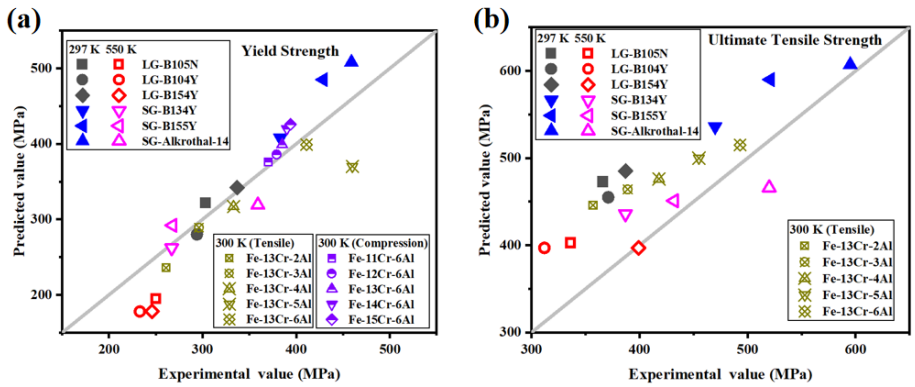

Figure 8. Comparisons of predicted properties with experimental data of different alloys and temperatures. **(a)** Yield strength and **(b)** Ultimate tensile strength. The large grain and small grain samples from [44] are denoted as LG-X and SG-X, respectively, where X means the specific alloy. The other experimental data are from [48].

At room temperature, all the predicted UTS are higher than the experimental data and the relative errors of the small grain samples are up to 14.1% which is lower than those of the large grain samples. At elevated temperature, small relative errors of the predicted UTS of small grain samples than the larger grain samples are also observed. Compared to the large grain samples, more uniform distribution of dislocation proliferation and better fracture toughness are shown in small grain samples during fracture. Based on the uniform elongation data, it is true that large grains are less ductile than small grains, which means that the values of G_i need to be adjusted for grain size, for example, the larger the grain size, the smaller the value of G_i. Overall, the accuracy of our proposed model is higher for small grain samples than for large grain ones, and covers different temperatures and multiple Cr and Al composition ranges.

To further improve the prediction accuracy of this model, more physical mechanisms could be considered such as intergranular fracture theory, which can establish the correlation between grain size and fracture behavior. In particular, a variety of classical simple phenomenological models are used in the multi-scale strategy in this study, and the number of parameters that need to be fitted are minimized. As more experimental data are accumulated, a comprehensive set of parameter candidate libraries will be gradually established from the perspective of top-down. At the same time, a more complete microscopic mechanism and the relationship between phenomenological parameters could be established by continuous refinement of the bottom-up model, especially by introducing machine learning interatomic potentials.

4.2. Application on MGI design

The input and output parameters of this multiscale coupling model meet the requirements of MGI design, enabling rapid prediction of alloy properties and genetic optimization in combination with machine learning techniques. Taking the Sample II recovery-FeCrAl alloy (annealing at 600 °C) as an example, the relationship between material genome inputs (composition and processing parameters) and key performance (YS) has been established. The selected material genome inputs include Cr content c_{Cr}^{wt} (11.0, 12.0, 13.0, 14.0, 15 wt%), Al content c_{Al}^{wt} (3.0, 3.5, 4.0, 4.5, 5.0 wt%), thickness reduction during rolling ε_{roll} (10, 20, 30, 40, 50, 60%), and annealing time during recovery t_{recov} (10, 20, 30, 40, 50, 60 min). This resulted in a total of $5 \times 5 \times 6 \times 6 = 900$ material genome input sets, brought into the multiscale model to obtain the computational dataset.

Based on this computational dataset, an artificial neural network (ANN) model is used to establish the mapping as $YS = f(c_{Cr}^{wt}, c_{Al}^{wt}, \varepsilon_{roll}, t_{recov})$. The prediction performance is illustrated in Figure 9a. The stability of the multiscale model results directly influences the agreement with ANN predictions. In the current multiscale model, the composition-related formula are deterministic, while randomness is only introduced during the grain structure initialization during the PFM simulations. This randomness leads to an error in YS of less than 1.5%, contributing to an excellent linear fit in the ANN predictions, with a correlation coefficient $R = 0.999$. Figure 9b,c show the influence of composition and processing parameters on the YS of the recovery FeCrAl alloy. The YS increases with c_{Cr}^{wt}, c_{Al}^{wt} and ε_{roll}, but decreases with t_{recov}. This example demonstrates that the multiscale model serves as a critical bridge between experimentation and Materials Genome Initiative. It enables a scalable data strategy—transitioning from several experimental data to extensive computational data, and finally to comprehensive predictive data—thereby achieving rapid performance prediction and facilitating material genome optimization of the nuclear-grade FeCrAl alloys.

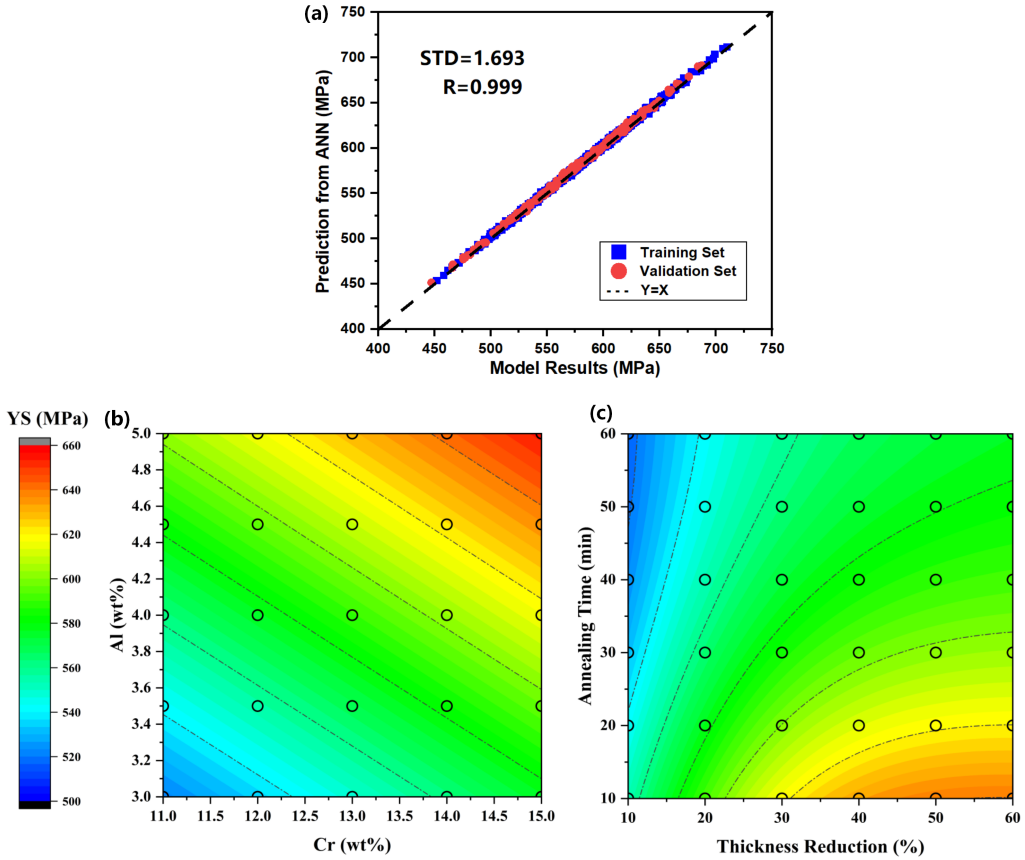

Figure 9. Prediction of yield strength using artificial neural network based on computational data. **(a)** Fitting analysis of the ANN training; **(b)** Effect of Cr and Al components with a fixed thickness reduction rate of 0.35 and annealing time of 35 minutes; **(c)** Influence of thickness reduction and annealing time on the YS of the cold-worked FeCrAl alloy, with a fixed weight composition of Fe-14Cr-4Al-1.92Mo-0.4Si. The hollow circles in **(b)** and **(c)** indicate the location of computational data from multiscale model.

5. Conclusions

This study establishes a feasible multi-scale model for calculating the mechanical properties of Fe-Cr-Al alloys, incorporating the effects of composition and processing. The model effectively integrates Molecular Dynamics, Phase-Field Method, and Finite Element Method across different scales within the framework of Crystal Plasticity theory. The main contributions are summarized as follows:

(1) A temperature-dependent Critical Resolved Shear Stress model is developed, capturing key plastic deformation mechanisms in Fe-Cr-Al alloys, such as dislocation-solute atom interactions, fracture of doped single crystals, and microstructural evolution during rolling and annealing.

(2) A bidirectional calibration strategy is implemented, which involves top-down parameter fitting from CPFEM, refinement of MD and solution strengthening models, and bottom-up calibration of PFM-related parameters.

(3) A robust, atomistically-informed solid solution hardening model for multi-component systems is proposed and validated.

(4) The model successfully predicts the polycrystalline structure and its corresponding mechanical response, which also elucidats the underlying microstructural evolution mechanisms.

(5) The multiscale coupling model serves as a bridge between experiment and Materials Genome Initiative, transforming limited experimental results into computational dataset of thousands, thereby enabling the creation of a database for machine learning and facilitating the prediction and optimization for MGI design.

Supplementary data

The authors confirm that the supplementary data are available within this article.

Acknowledgments

The authors acknowledge the National Key Research and Development Program of China (Grant No. 2016YFB0700100, 2024YFB3817300), the National Natural Science Foundations of China (Grant Nos. 12105066, 52250005, 21875271, U20B2021, 21707147, 51372046, 51479037, 91226202, and 91426304), the Key Research and Development Projects of Zhejiang Province (Nos. 2022C01236 and 2019C01060), the YangtzeDelta Region Institute (Huzhou) Guidance Fund of University of Electronic Science and Technology of China (No. U03250002), the Science and Technology Innovation 2025 Major Project of Ningbo (2024Z284), and the Zhejiang Key Laboratory of Data-Driven High-Safety Energy Materials and Applications.

Authors' contribution

Conceptualization, Shiyu Du and Shurong Ding; methodology, Zhen Liu, Yaolin Guo and Jingyu Zhang; software, Zhen Liu, Yaolin Guo, Jingyu Zhang and Zheyu Hu; validation, Zhen Liu, Yaolin Guo, Jingyu Zhang and Yifan Li; formal analysis, Zhen Liu, Yaolin Guo and Jingyu Zhang; investigation, Zhen Liu, Yaolin Guo, Jingyu Zhang and Muhammad Adnan; resources, Shiyu Du and Shurong Ding; data curation, Nianxiang Qiu; writing—original draft preparation, Zhen Liu, Yaolin Guo and Jingyu Zhang; writing—review and editing, Nianxiang Qiu, Yifan Li, Zheyu Hu, Muhammad Adnan, Shiyu Du and Shurong Ding; visualization, Zhen Liu and Jingyu Zhang; supervision, Yaolin Guo, Shiyu Du and Shurong Ding; project administration, Yaolin Guo; funding acquisition, Shiyu Du. All authors have read and agreed to the published version of the manuscript.

Conflicts of interests

Shiyu Du holds the position of Honorary Editors-in-Chief for AI & Materials and has not peer reviewed or made any editorial decisions for this paper.

Appendix A. MD-assisted solution strengthening models

Based on the screw dislocation kink pair nucleation and migration mechanisms, Argon [25] has provided the formula for τ_{ss}^{screw} (superscript α in Section 2.1 has been dropped) in order to separately consider the influence of concentration c and temperature T, written as

$$\tau_{screw}(T,c) = \hat{\tau}_s^{km}(c)\left(1-\left(\frac{k_B T}{\Delta E_s^{km}(c)}\ln\left(\frac{\dot{\varepsilon}_0}{\dot{\varepsilon}}\right)\right)^{2/3}\right)+\tau_s^{ath}(c) \tag{A.1}$$

where $\dot{\varepsilon}_0$ is the reference strain rate, $\dot{\varepsilon}$ is the loading strain rate, k_B is the Boltzmann constant, $\Delta E_s^{km}(c)$ is the kink migration energy barrier, $\hat{\tau}_s^{km}(c)$ is the resistance due to the kink migration process at 0 K and $\tau_s^{ath}(c)$ denotes the athermal resistance stress. It is worth noted that all the parameters in Argon's model are considered to be temperature independent and take values at 0 K. $\tau_s^{ath}(c)$, $\Delta E_s^{km}(c)$ and $\tau_s^{ath}(c)$ are respectively expressed as [25]

$$\begin{aligned} \Delta E_s^{km}(c) &= \left(\sum_{X=Cr,Al,\ldots} \left(m_0^X(c_X) \Delta U_{screw}^X \right)^2 \right)^{1/2} \\ \hat{\tau}_s^{km}(c) &= 0.572 \left(\frac{\Delta E_s^{km}(c)}{b \lambda_s w_k} \right) \\ \tau_s^{ath}(c) &= \sum_{X=Cr,Al,\ldots} 0.858 \frac{\Delta U_{screw}^X}{{w_s}^2 b} c + \tau_{s,Fe}^{ath} \end{aligned} \tag{A.2}$$

where c_X is the atomic concentration for solute element X (such as Cr, Al, *etc.*), b is the magnitude of Burgers vector $\mathbf{b}$, w_k is the average kink-pair twist width, $m_0^X(c_X)$ is the average number of solution atoms contained in a screw dislocation segment, λ_s is the nearest distance of Peierls valley of screw dislocations, w_s is the interaction range between screw dislocations with solute atoms, and $\tau_{s,Fe}^{ath}$ is the non-thermal lattice resistance stress for pure iron. Here, $m_0^X(c_X)$ is taken as $25\sqrt{c_X}$, which is estimated for Fe-based alloy with a mobile dislocation density of $10^{12}/\mathrm{m}^2$ [49]. ΔU_{screw}^X is the energy barrier for screw-kink migration over single substitutional defect, simply estimated as the maximum energy difference as

$$\Delta U_{screw}^X = \max_i^N \{ U_{screw}^X(\mathbf{r}_i + n_s \mathbf{b}) - U_{screw}^X(\mathbf{r}_i) \} \tag{A.3}$$

where N denotes the representative number of atomic sites involved in the kink migration process, n_s is a positive integer to estimate the migration distance and $\mathbf{b}$ is the Burgers vector. Notably, $U_{screw}^X(\mathbf{r}_i)$ is the binding energy of screw dislocation and solute element X at atomic site $\mathbf{r_i}$, defined as

$$U_{dis}^X(\mathbf{r}_i) = E_{dis}^X(\mathbf{r}_i) - E_{dis}^{X,\,ref} \tag{A.4}$$

where $E_{dis}^X(\mathbf{r}_i)$ refers to the total energy for X substitution defect at atomic site $\mathbf{r_i}$ near the dislocation core and $E_{dis}^{X,\,ref}$ is the reference total energy for X substitution defect far away from dislocation core.

As for the solution strengthening effect associated with edge dislocations, since the annealing temperature is also included, the Leyson developed Labusch model for high temperature [50,51,26] is applied to describe τ_{ss}^{edge} as

$$\tau_{edge}(T,c) = \hat{\tau}_e(c) \exp\left(-\frac{1}{0.55} \frac{k_B T}{\Delta E_e(c)} \ln\left(\frac{\dot{\varepsilon}_0}{\dot{\varepsilon}} \right) \right) \tag{A.5}$$

where $\hat{\tau}_e(c)$ and $\Delta E_e(c)$ are the flow stress and energy barrier for edge dislocation migration and have the following relationship

$$\hat{\tau}_e(c) = \frac{\pi \Delta E_e(c)}{2 b w_e^{crit} \zeta_e^{crit}(w_e^{crit})} \tag{A.6}$$

Here w_e^{crit} and $\zeta_e^{crit}(w_e^{crit})$ are the critical amplitude and length of the wave shaped edge dislocation segment. According to Maresca's model [30] for BCC alloys, the relationship between w_e^{crit} and $\zeta_e^{crit}(w_e^{crit})$ is

$$\zeta_e^{crit}(w_e^{crit}) = 1.73\left(\frac{{\Gamma_e}^2 {w_e^{crit}}^4 b}{\Delta\tilde{E}_p(c, w_e^{crit})^2}\right)^{1/3} \tag{A.7}$$

where Γ_e is the edge dislocation line tension and $\Delta\tilde{E}_p(c, w_e^{crit})$ is the energy increment caused by the wavy edge dislocation interaction with the random solute defects. Assuming that w_e^{crit} is related to the edge dislocation core structure and independent on the solute element, $\Delta\tilde{E}_p(c, w_e^{crit})$ in the multi solute elements system can be calculated as accumulation from single solute systems, expressed as

$$\Delta\tilde{E}_p(c, w_e^{crit}) = \left[\sum_X c_X \Delta\tilde{E}_p^X(w_e^{crit})^2\right]^{1/2} \tag{A.8}$$

where $\Delta\tilde{E}_p^X(w_e^{crit})$ is the characteristic energy to evaluate the pinning effects of solute element X. $\Delta\tilde{E}_p^X(w_e)$ is calculated as the statistical energy for the edge dislocation segment with the unit length $2\sqrt{2}b$ gliding towards with the distance of wave amplitude w_e, expressed as

$$\Delta\tilde{E}_p^X(w_e) = \left[\sum_i^N \left(U_{edge}^X(\mathbf{r}_i + \frac{w_e}{b}\mathbf{b}) - U_{edge}^X(\mathbf{r}_i)\right)^2\right]^{1/2} \tag{A.9}$$

where N denotes the representative number of atomic sites near the edge dislocation core and $U_{edge}^X(\mathbf{r}_i)$ is the binding energy of edge dislocation and solute element X, as defined in Equation (A.1). The critical wave amplitude w_e^{crit} is determined by minimizing $\Delta\tilde{E}_{tot}(w_e)$ (the total energy of wavy edge dislocation segment for unit length), which is calculated as

$$\Delta\tilde{E}_{tot}(w_e) = -0.274\left(\frac{\Delta\tilde{E}_p^X(w_e)^4}{b^2 w_e \Gamma_e}\right)^{1/3} \tag{A.10}$$

w_e^{crit} is taken as the average value from all the Fe-X single solute systems.

For the edge dislocation migration energy barrier, $\Delta E_e(c)$ is calculated as $\Delta E_e(c) = 1.11\left(\Delta\tilde{E}_p(c, w_e^{crit})^2 \Gamma_e {w_e^{crit}}^2 / b\right)^{1/3}$ in original Maresca's model and the energy barrier and flow stress for pure edge dislocation ($c = 0$) are ignored, thus $\Delta E_e(0) = 0, \hat{\tau}_e(0) = 0$. However, the Peierls stress $\hat{\tau}_e(c)$ for BCC iron is nonnegligible (the theoretical and simulated value is around 60–65 MPa [39]). Therefore, the formula for $\Delta E_e(c)$ is modified at $c = 0$ to ensure the value of $\hat{\tau}_e(0)$ follows

$$\Delta E_e(c) = \frac{2b w_e^{crit} \zeta_e^c}{\pi}\hat{\tau}_e(0) + 1.11\left(\frac{\Delta\tilde{E}_p(c, w_e^{crit})^2 \Gamma_e {w_e^{crit}}^2}{b}\right)^{1/3} \tag{A.11}$$

Furthermore, since the volumetric term dominates $U_{dis}^X(r)$ for edge dislocations while the chemical term is negligible [30], the volumetric misfit approximation model—simplified from Yasi's model [42]—is employed. This model reduces the dependency on interatomic potentials and is used here in place of Equation (A.6). Specifically, the VMA for $U_{edge}^X(\mathbf{r})$ is calculated as

$$U_{edge}^X(\mathbf{r}) = -3BV_0 \Delta V(\mathbf{r}) \varepsilon_a^X \tag{A.12}$$

where B is bulk modulus, V_0 is the atomic volume in bulk, $\Delta V(\mathbf{r}) = (V(\mathbf{r}) - V_0)/V_0$ is the volumetric difference of the atomic sites near dislocation core, and ε_a^X is the size misfit parameter in the bulk and

calculated as $\varepsilon_a^X = \left(1/a \times da/dc_X\right)_{c_X=0}$ with the lattice parameter a.

Appendix B. CP-PFM coupled models for rolling-annealing processes

First, FFT-CP model [36] is used to simulate the rolling process, the basic framework of which is similar to the previous CP model, except that it is solved by the FFT method under periodic boundary conditions. The FFT-CP used in this article is briefly described as follows. An average velocity gradient $V_{i,j}$ is imposed in the simulation block and decomposed into two parts as (1) an average strain-rate $\dot{E}_{ij} = (V_{i,j} + V_{j,i})/2$ and (2) average rotation-rate $\dot{\Omega}_{ij} = (V_{i,j} - V_{j,i})/2$. The local strain-rate field $\dot{\varepsilon}_{ij}(\mathbf{x})$ is split into its average $\dot{E}_{ij}$ and a fluctuation term $\tilde{\dot{\varepsilon}}_{ij}$, i.e., $\dot{\varepsilon}_{ij} = \dot{E}_{ij} + \tilde{\dot{\varepsilon}}_{ij}$. The local constitutive relation for each material point between the strain-rate $\dot{\varepsilon}_{ij}$ and the deviatoric stress $\boldsymbol{\sigma}'(\mathbf{x})$ is given by the classic incompressible rate-dependent crystal plasticity equation [36]:

$$\dot{\varepsilon}_{ij}(x) = \sum_{\alpha=1}^{N_\alpha} m_{ij}^\alpha(\mathbf{x})\dot{\gamma}^\alpha(\mathbf{x}) \tag{B.1}$$

where $\mathbf{m}^\alpha = (\mathbf{n}^\alpha(\mathbf{x}) \otimes \mathbf{b}^\alpha(\mathbf{x}) + \mathbf{b}^\alpha(\mathbf{x}) \otimes \mathbf{n}^\alpha(\mathbf{x}))/2$ is the symmetric Schmid tensor, and the shear strain rate $\dot{\gamma}^\alpha(\mathbf{x})$ can be calculated by Eq.(1) with $\tau^\alpha = m^\alpha(\mathbf{x}) : \boldsymbol{\sigma}'(\mathbf{x})$. The non-linear hardening model adopted in FFT-CP is exactly the same as equations in Section 2.1, like Equation (1). Although FFT-CP does not model the changes in grain morphology involved, it can give accumulated plastic strain and τ_c^α during rolling process, which is vital for the subsequent simulation of recovery and recrystallization during annealing.

To simulate the process of recovery, second, Verdier's model with respect to CRSS changing rate $\dot{\tau}_c^\alpha$ is adopted as [52]

$$\dot{\tau}_c^\alpha(\mathbf{x}) = -\frac{E\rho(\mathbf{x})b^2\upsilon_D}{M(\mathbf{x})} \exp\left(-\frac{U_0}{k_B T}\right) \sinh\left(\frac{\tau_c^\alpha \nu}{k_B T}\right) \tag{B.2}$$

where E is the Young's modulus, υ_D is the Debye frequency. Furthermore, $\rho(\mathbf{x}) = \sum_\alpha^{N_\alpha} \left(\tau_c^\alpha(\mathbf{x})/M(\mathbf{x})Gb\right)^2$ is employed to estimate the dislocation density, where $M(\mathbf{X})$ is the Taylor factor which can be calculated according to the results of FFT-CP. U_0 and ν are respectively the activation energy and volume for dislocation motion during recovery process, which should be determined according to the dominate mechanism responsible for the recovery process, for instance, self-diffusion.

Third, the Multi-Phase-Field (MPF) model considering plastic energy is used for the simulation of recrystallization with the free energy functional written as [16]

$$F = \int_V \left[\sum_{i=1}^{N_g}\sum_{j=i+1}^{N_g}\left(-\frac{a_{ij}^2}{2}\nabla\phi_i \cdot \nabla\phi_j + W_{ij}\phi_i\phi_j\right) + f_{vp}\right] dV \tag{B.3}$$

where a_{ij} is the gradient coefficient, W_{ij} is the height of the energy barrier between grains i and j, f_{vp} is the plastic energy in a polycrystalline system containing N_g grains. The i-th grain can be indicated by phase field ϕ_i which initially takes a value of 1 inside the i-th grain, 0 in the other grains and $0 < \phi_i < 1$ at the grain boundary. ϕ_i should satisfy the condition as $\sum_{i=1}^{N_g} \phi_i = 1$. The governing equation of the phase field ϕ_i is expressed as

$$\frac{\partial \phi_i}{\partial t} = -\sum_{j=1}^{n} \frac{2M_{ij}^{\phi}}{n}\left(\frac{\delta F}{\delta \phi_i} - \frac{\delta F}{\delta \phi_j}\right) \tag{B.4}$$

where $\delta()$ denotes variational derivative, n represents the number of involved grains at interfaces which can be calculated as $n = \sum_{i=1}^{N_g} \eta_i$ with $\eta_i = 1$ when $0 < \phi_i \leq 1$ and 0 otherwise, M_{ij}^{ϕ} is the phase field mobility. Normally, the biggest component of phase field is called the principal one. In the numerical implementation, up to 8 phase field components ($n \leq 8$) are employed to fully simulate the process of grain growth with the approach proposed by [37] to lower the computational expense. Based on the asymptotic analysis of multiphase field model, these parameters can be related to the interface properties of materials. The coefficients α_{ij}, W_{ij} and M_{ij}^{ϕ} in the equation can be connected with grain boundary properties, including the thickness δ_{ij}, energy γ_{ij} and mobility M_{ij}, respectively, written as

$$a_{ij} = \frac{2}{\pi}\sqrt{2\delta_{ij}},\ W_{ij} = \frac{4\gamma_{ij}}{\delta_{ij}},\ M_{ij}^{\phi} = \frac{\pi^2}{8\delta_{ij}} M_{ij} \tag{B.5}$$

Specifically, γ_{ij} is evaluated by the MD simulation at the atomic scale. According to the classical CP theory, plastic energy is uniquely determined by $\tau_c^{\alpha}(\mathbf{x},t)$ and shear strain $\gamma^{\alpha}(\mathbf{x},t)$. If the deformation is assumed to be small and the linear hardening model is considered, based on the work of [16], the plastic energy can be expressed as

$$f_{vp}^{Chen} = \int \sum_{\alpha=1}^{N_\alpha} \tau^{\alpha}(\mathbf{x},t)\Delta\gamma^{\alpha}(\mathbf{x},t)dt = \tau_{c,0}^{\alpha}(\mathbf{x},0)M(\mathbf{x})\varepsilon_{vM}(\mathbf{x}) + HM^2(\mathbf{x})[\varepsilon_{vM}(\mathbf{x})]^2/2 \tag{B.6}$$

where $M(\mathbf{x})$ is calculated at time t through accumulated shear strain $\Delta\gamma(\mathbf{x},t)$ and the von Mises strain $\Delta\varepsilon_{vM}(\mathbf{x},t)$, *i.e.*, $\Delta\gamma(\mathbf{x},t)/\Delta\varepsilon_{vM}(\mathbf{x},t)$, and vM is short for von Mises. $\varepsilon_{vM}(\mathbf{x})$ is the synthesized von Mises strain by combining ϕ_i and an effective von Mises $\varepsilon_{i,vM}(\mathbf{x})$, *i.e.*, $\varepsilon_{vM}(\mathbf{x}) = \sum_i(-2\phi_i^3 + 3\phi_i^2)\varepsilon_{i,vM}(\mathbf{x})$. As the critical parameter connecting the FFT-CP results and the phase field model, $\varepsilon_{i,vM}(\mathbf{x})$ is calculated following the work of [16], that is, the principal component is taken directly as $\varepsilon_{vM}(\mathbf{x})$ from FFT-CP, while the other components use the average strain in the corresponding grains, and more details can be found in [16]. The linear expression in Equation (B.6) makes it desirable to get analytical expressions of the relationship between order parameters and plastic strain. Since a non-linear hardening model is adopted for actual materials, the calculation of plastic energy has to be modified accordingly. At this moment, an effective linear hardening coefficient $\bar{H}$ is introduced to describe the stress-strain relationship after the plastic working process, estimated as

$$\bar{H} = \frac{1}{N_g N_\alpha}\sum_{i}^{N_g}\sum_{\alpha}^{N_\alpha}(\Delta\tau_{vM}^{\alpha}/\gamma_{vM}^{\alpha}) \tag{B.7}$$

where $\Delta\tau_{vM}^{\alpha}$ is the actual stress increment during the whole plastic deformation process, γ_{vM}^{α} denotes the shear strain at the end of the deformation, at each slip system. Besides, an energy dissipation factor λ is introduced to represent the significant energy dissipation which should not be ignored when the deformation is large. Therefore, the newly established f_{vp} can be written as

$$f_{vp} = \lambda\left(\tau_{c,0}^{\alpha}(\mathbf{x},0)M(\mathbf{x})\varepsilon_{vM}(\mathbf{x}) + \frac{1}{2}\bar{H}M^2(\mathbf{x})[\varepsilon_{vM}(\mathbf{x})]^2\right) \tag{B.8}$$

When recrystallization occurs, the new grains will be directly assigned a strain of 0, they will gain much driving force to migrate, resulting in the changing of strain distribution and finally the implementation of recrystallization in polycrystalline system.

Appendix C. CPFEM-based polycrystal mechanical model

The models in our previous work [4] are adopted to conduct the CPFEM, and they are briefly summarized here. The constitutive model for each material point in each grain is expressed as

$$\begin{aligned}
\hat{\sigma} &= (1-d)\,\hat{\mathbf{C}}^0 : (\hat{\varepsilon} - \hat{\varepsilon}^p) \\
\hat{\varepsilon} &= \int \left(\hat{\bar{\mathbf{R}}}^{\mathrm{T}} \cdot \mathbf{D} \cdot \hat{\bar{\mathbf{R}}} \right) \mathrm{d}t \\
\hat{\varepsilon}^p &= \int \left(\sum_{\alpha=1}^{N_\alpha} \dot{\gamma}^{(\alpha)} \hat{\mathbf{P}}^{(\alpha)} \right) \mathrm{d}t \\
\hat{\bar{\mathbf{R}}} &= \bar{\mathbf{R}} \cdot \mathbf{R}_0 \\
\hat{\mathbf{P}}^{(\alpha)} &= \mathbf{R}_0^{\mathrm{T}} \cdot \mathrm{sym}(\mathbf{n}_0^{(\alpha)} \otimes \mathbf{b}_0^{(\alpha)}) \cdot \mathbf{R}_0
\end{aligned} \tag{C.1}$$

where $\hat{\sigma}$ is the co-rotational Cauchy stress, d is the damage factor same as that in Equation (2), $\hat{\mathbf{C}}^0$ is the fourth-order co-rotational elastic tensor, $\hat{\varepsilon}$ is the co-rotational total strain, $\hat{\varepsilon}^p$ is the plastic strain tensor, $\bar{\mathbf{R}}$ represents rigid body motion, D is the rate-of-deformation, $\dot{\gamma}^{(\alpha)}$ is the shear strain rate and is obtained according to Equation (1), $\mathbf{R}_0$ depicts the initial orientation of the grain, "sym" denotes the symmetrical part of a tensor, $\mathbf{b}_0^{(\alpha)}$ is the slip direction and $\mathbf{n}_0^{(\alpha)}$ is the normal direction the slip plane in initial configuration.

After the simulation by CPFEM, the homogenized true stress is obtained by volume-averaged Cauchy stress, $\bar{\sigma}$, that is [4]

$$< \sigma >= \frac{1}{V}\int_V \sigma \,\mathrm{d}V = \frac{1}{V}\int_V \left(\hat{\bar{\mathbf{R}}} \cdot \hat{\sigma} \cdot \hat{\bar{\mathbf{R}}}^{\mathrm{T}} \right) \mathrm{d}V \tag{C.2}$$

where V is the volume of the RVE in current configuration. The homogenized engineering strain is obtained by using the nodal displacement of the RVE [4]. Then the true stresses are converted to engineering stresses. The macroscopic effective elastic modulus is the slope of the stress-strain curve in the elastic deformation stage. The yield strength is obtained by using the stress when the plastic strain is 0.2%, and the UTS is determined as the maximum engineering stress.

References

[1] Gong M, Xie D, Sun T, Zhang X, Shao L, *et al.* Bridging microscale to macroscale mechanical property measurements of FeCrAl alloys by crystal plasticity modeling. *Int. J. Plast.* 2023, 165:103608.

[2] Pachaury Y, Warren G, Wharry JP, Po G, El-Azab A. Plasticity in irradiated FeCrAl nanopillars investigated using discrete dislocation dynamics. *Int. J. Plast.* 2023, 167:103676.

[3] Field KG, Snead MA, Yamamoto Y, Terrani KA. Handbook on the material properties of FeCrAl alloys for nuclear power production applications. 2018. Available: https:https://info.ornl.gov/sites/publications/Files/Pub114121.pdf (accessed on 20 July 2025).

[4] Zhang J, Ding S, Du S. A damage-effect-involved phenomenological crystal plasticity model and computational methods for mechanical responses of FeCrAl alloys. *Mater. Today Commun.* 2021, 28:102595.

[5] The development of cladding materials for the accident tolerant fuel system from the materials genome initiative. *Scr. Mater.* 2017, 141:99–106.

[6] Pouriayevali H, Xu B. Decomposition of dislocation densities at grain boundary in a finite-deformation gradient crystal-plasticity framework. *Int. J. Plast.* 2017, 96:36–55.

[7] Lin P, Nie J, Lu Y, Shi C, Cui S, *et al.* Atomic irradiation defects induced hardening model in irradiated tungsten based on molecular dynamics and CPFEM. *Int. J. Plast.* 2024, 174:103895.

[8] Segurado J, Lebensohn RA, Llorca J. Computational homogenization of polycrystals. *Adv. Appl. Mech.* 2018, 51:1–114.

[9] Upadhyay MV, Patra A, Wen W, Panzner T, Van Petegem S, *et al.* Mechanical response of stainless steel subjected to biaxial load path changes: cruciform experiments and multi-scale modeling. *Int. J. Plast.* 2018, 108:144–168.

[10] Lim H, Battaile CC, Carroll JD, Boyce BL, Weinberger CR. A physically based model of temperature and strain rate dependent yield in BCC metals: implementation into crystal plasticity. *J. Mech. Phys. Solids* 2015, 74:80–96.

[11] Zhao F, Liu W, Yi X, Zhang Y, Duan H. Multiscale modeling of dislocation-mediated plasticity of refractory high entropy alloys. *J. Mech. Phys. Solids* 2024, 187:105640.

[12] Liu F, Liu Z, Pei X, Hu J, Zhuang Z. Modeling high temperature anneal hardening in Au submicron pillar by developing coupled dislocation glide-climb model. *Int. J. Plast.* 2017, 99:102–119.

[13] Groh S, Marin E, Horstemeyer M, Zbib H. Multiscale modeling of the plasticity in an aluminum single crystal. *Int. J. Plast.* 2009, 25(8):1456–1473.

[14] Asgharzadeh A, Nazari Tiji SA, Park T, Pourboghrat F. Prediction of softening kinetics and recrystallization texture in non-isothermally annealed bulged tubes using CPFEM and CA models. *Mater. Sci. Eng. A* 2022, 832:142308.

[15] Yao S, Yu J, Pei X, Cui Y, Zhang H, *et al.* A coupled phase-field and crystal plasticity model for understanding shock-induced phase transition of iron. *Int. J. Plast.* 2024, 173:103860.

[16] Chen L, Chen J, Lebensohn RA, Ji Y, Heo TW, *et al.* An integrated fast Fourier transform-based phase-field and crystal plasticity approach to model recrystallization of three dimensional polycrystals. *Comput. Methods Appl. Mech. Eng.* 2015, 285:829–848.

[17] Zhao P, Low TSE, Wang Y, Niezgoda SR. An integrated full-field model of concurrent plastic deformation and microstructure evolution: application to 3D simulation of dynamic recrystallization in polycrystalline copper. *Int. J. Plast.* 2016, 80:38–55.

[18] Mo H, Liu G, Mao Y, Shen Y, Wang J. Dual-interface model for twinning in the coupled crystal plasticity finite element—phase field method. *Int. J. Plast.* 2022, 158:103441.

[19] Min KM, Lee H, Joo HD, Han HN, Lee MG. Numerical modeling of shear band effect on Goss grain recrystallization in electrical steels: crystal plasticity finite element and phase field modeling. *Int. J. Plast.* 2024, 180:104049.

[20] Xiao X, Terentyev D, Yu L, Song D, Bakaev A, *et al.* Modelling irradiation-induced softening in

BCC iron by crystal plasticity approach. *J. Nucl. Mater.* 2015, 466:312–315.

[21] Sun Z, Yamamoto Y. Processability evaluation of a Mo-containing FeCrAl alloy for seamless thin-wall tube fabrication. *Mater. Sci. Eng. A* 2017, 700:554–561.

[22] Lee C, Maresca F, Feng R, Chou Y, Ungar T, *et al.* Strength can be controlled by edge dislocations in refractory high-entropy alloys. *Nat. Commun.* 2021, 12(1):5474.

[23] Ji R, Phan T, Chen H, Xiong L. Quantifying the dynamics of dislocation kinks in iron and tungsten through atomistic simulations. *Int. J. Plast.* 2020, 128:102675.

[24] Kumar P, Ludhwani MM, Das S, Gavini V, Kanjarla A, *et al.* Effect of hydrogen on plasticity of -Fe: a multi-scale assessment. *Int. J. Plast.* 2023, 165:103613.

[25] Argon AS. *Strengthening Mechanisms in Crystal Plasticity*, 1st ed. Oxford: Oxford University Press, 2008.

[26] Varvenne C, Leyson M, Ghazisaeidi M, Curtin W. Solute strengthening in random alloys. *Acta Mater.* 2017, 124:660–683.

[27] Kim JB, Yoon JW. Necking behavior of AA 6022-T4 based on the crystal plasticity and damage models. *Int. J. Plast.* 2015, 73:3–23.

[28] Huang X, Wang H, Qiu S, Zhang Y, He K, *et al.* Cold-rolling annealing process for nuclear grade wrought FeCrAl cladding alloy to enhance the strength and ductility. *J. Mater. Process. Technol.* 2020, 277:116434.

[29] Pogorelko VV, Mayer AE. Dynamic tensile fracture of iron: molecular dynamics simulations and micromechanical model based on dislocation plasticity. *Int. J. Plast.* 2023, 167:103678.

[30] Maresca F, Curtin WA. Mechanistic origin of high strength in refractory BCC high entropy alloys up to 1900 K. *Acta Mater.* 2020, 182:235–249.

[31] Brown SB, Kim KH, Anand L. An internal variable constitutive model for hot working of metals. *Int. J. Plast.* 1989, 5(2):95–130.

[32] Terentyev D, Bonny G, Domain C, Pasianot RC. Interaction of a $\frac{1}{2}\langle 111\rangle$screw dislocation with Cr precipitates in bcc Fe studied by molecular dynamics. *Phys. Rev. B* 2010, 81(21):214106.

[33] Queyreau S, Marian J, Gilbert MR, Wirth BD. Edge dislocation mobilities in bcc Fe obtained by molecular dynamics. *Phys. Rev. B* 2011, 84(6):064106.

[34] Shibuta Y, Takamoto S, Suzuki T. A molecular dynamics study of the energy and structure of the symmetric tilt boundary of iron. *ISIJ Int.* 2008, 48(11):1582–1591.

[35] Guo Y, Li Y, Liu Z, Shi D, Song J, *et al.* Development of a phase field tool coupling with thermodynamic data for microstructure evolution simulation of alloys in nuclear reactors. *Front. Mater.* 2021, 8:627864.

[36] Lebensohn RA, Brenner R, Castelnau O, Rollett AD. Orientation image-based micromechanical modelling of subgrain texture evolution in polycrystalline copper. *Acta Mater.* 2008, 56(15):3914–3926.

[37] Kim SG, Kim DI, Kim WT, Park YB. Computer simulations of two-dimensional and three-dimensional ideal grain growth. *Phys. Rev. E* 2006, 74(6):061605–061618.

[38] Wakeda M, Tsuru T, Kohyama M, Ozaki T, Sawada H, *et al.* Chemical misfit origin of solute strengthening in iron alloys. *Acta Mater.* 2017, 131:445–456.

[39] Liu Z, Guo Y, Li Y, Qiu N, Zhang J, *et al.* MS-informed misfit approximation model for the

interaction energy between substitutional atoms and screw dislocations in BCC iron-based alloys. *Comput. Mater. Sci* 2024, 241:113031.

[40] Leslie WC. Iron and its dilute substitutional solid solutions. *Metall. Mater. Trans. B* 1972, 3:5–26.

[41] Takeuchi, Shin. Solid-solution strengthening in single crystals of iron alloys. *J. Phys. Soc. Jpn.* 1969, 27(4):929–940.

[42] Yasi JA, Hector LG, Trinkle DR. First-principles data for solid-solution strengthening of magnesium: from geometry and chemistry to properties. *Acta Mater.* 2010, 58(17):5704–5713.

[43] Ghosh G, Olson GB. The isotropic shear modulus of multicomponent Fe-base solid solutions. *Acta Mater.* 2002, 50(10):2655–2675.

[44] Yamamoto Y, Pint BA, Terrani KA, Field KG, Yang Y, *et al.* Development and property evaluation of nuclear grade wrought FeCrAl fuel cladding for light water reactors. *J. Nucl. Mater.* 2015, 467:703–716.

[45] Martınez-de Guerenu A, Arizti F, Gutiérrez I. Recovery during annealing in a cold rolled low carbon steel. Part II: modelling the kinetics. *Acta Mater.* 2004, 52(12):3665–3670.

[46] Mavrikakis N, Detlefs C, Cook PK, Kutsal M, Campos APC, *et al.* A multi-scale study of the interaction of Sn solutes with dislocations during static recovery in -Fe. *Acta Mater.* 2019, 174:92–104.

[47] Qin X, Zhang R, Du P, Pei J, Pan Q, *et al.* Recrystallization and texture evolution of cold pilgered FeCrAl cladding tube during annealing at 700 °C–1000 °C. *J. Nucl. Mater.* 2023, 577:154303.

[48] Wang P, Qiao Y, Qi W, Du S, Liu Z, *et al.* Preparation and properties study of Cr on FeCrAl cladding materials. *Front. Mater.* 2021, 8:47.

[49] Trinkle DR, Woodward C. The chemistry of deformation: how solutes soften pure metals. *Science* 2005, 310(5754):1665–1667.

[50] Leyson GPM, Hector LG, Curtin WA. Solute strengthening from first principles and application to aluminum alloys. *Acta Mater.* 2012, 60(9):3873–3884.

[51] Leyson GPM, Curtin WA. Solute strengthening at high temperatures. *Modell. Simul. Mater. Sci. Eng.* 2016, 24(6):065005.

[52] Verdier M, Brechet Y, Guyot P. Recovery of AlMg alloys: flow stress and strain-hardening properties. *Acta Mater.* 1998, 47(1):127–134.